Seismic attenuation in Antarctic firn

Stefano Picotti[1], José M. Carcione[1,2], and Mauro Pavan[3]

[1]National Institute of Oceanography and Applied Geophysics (OGS), Trieste, Italy.
[2]School of Earth Sciences and Engineering, Hohai University, Nanjing, China.
[3]University of Genova, Italy.

Correspondence: Stefano Picotti (spicotti@ogs.it)

Abstract.

We estimate the P- and S-wave seismic attenuation in polar firn from spectral analysis of diving-wave first-breaks of three-component active-source seismic observations carried out in 2010 on the Whillans Ice Stream (WIS), a fast-flowing ice stream in West Antarctica. The resulting quality factors are then successfully modeled using a rock-physics theory of wave propagation which combines White's mesoscopic attenuation theory of interlayer flow with that of Biot/squirt flow. The first theory describes an equivalent viscoelastic medium of a stack of two thin alternating porous layers of thickness much larger than the pore size but smaller than the wavelength. On the other hand, in the so-called Biot/squirt-flow model, there are two loss mechanisms, namely the Biot global-flow one and local flow from fluid-filled micro-cracks (or grain contacts) to the pore space and back, where the former is dominant over the latter. The fluid saturating the pores is assumed to be fluidized snow, which is defined as a mixture of snow particles and air, like powder, having zero rigidity modulus.

1 Introduction

The shallow part of polar ice sheets and ice streams, commonly known as firn, is subjected to snow densification, a metamorphic process activated by the pressure gradient due to the accumulation of snow and by the temperature gradient at the near surface (Wilkinson, 1988). As a result, the density of firn increases continuously from the surface to the pore close-off depth, where the material can be considered glacial ice (Herron and Langway, 1980). Below this depth, the compression of englacial bubbles further increases the ice density until the maximum value is reached. In the very cold and dry internal parts of the Antarctic continent, the densification is slow and the firn layer thickness exceed 100 m (van den Broeke, 2008). On the other hand, in the high-strain shear margins of ice streams, this metamorphic process can be enhanced due to the effect of strain softening (Oraschewski and Grinsted, 2022), leading to exceptionally thin firn layers.

Because of its density structure, polar firn is generally laterally homogeneous with the seismic velocity increasing non-linearly with depth. This velocity profile results in a continuous refraction of seismic waves (Greenhalgh and King, 1981), which are also called diving waves. There are several examples in the literature, that used diving waves to resolve the firn velocity-depth structure by picking and inverting the first-break traveltimes (e.g., Kirchner and Bentley, 1979; King and Jarvis, 2007; Picotti et al., 2015). However, to our best knowledge, there are no examples of vertical profiling and modeling of intrinsic seismic attenuation of P and S waves in polar firn, so far.

Intrinsic loss is often quantified using the inverse quality factor $1/Q$, which represents the fraction of wave energy lost to heat in each wave period (e.g., Carcione, 2022; Gurevich and Carcione, 2022). P-wave quality factors (Q_P) in ice have been measured by several authors, from values as low as 5 in temperate ice of mountain glaciers (e.g., Gusmeroli and others, 2010) up to 700 in cold polar ice sheets (e.g., Bentley and Kohnen, 1976). This wide range indicates a strong dependance

30 of the quality factor on temperature, further verified in Peters et al. (2012) by seismic measurements in Greenland, where Q_P decreases with depth due to an increase in temperature. This dependence has also been demonstrated by laboratory experiments (e.g., Kuroiwa, 1964). Regarding the S-wave quality factor (Q_S), Clee et al. (1969) and Carcione et al. (2021) measured Q_S in warm ice of mountain glaciers, reporting values of about 23 and 12, respectively. To the best of our knowledge, no other measurements of Q_S in glacial ice or firn were published in the literature.

35 While cold polar ice attenuation is very low, this is not the case of polar firn. Bentley and Kohnen (1976) obtained a value of the ice P-wave quality factor from seismic refraction measurements at Byrd Station of about 715 at 136 Hz, between 100 m and 500 m depth and at an average temperature of about -28 °C. Because this value is very high, intrinsic attenuation in polar ice (below the firn) is a minor factor in reducing the signal amplitude, in their case. On the other hand, Albert (1998) performed numerical simulations of seismic waves in firn at the South Pole, Antarctica, between 0 and 300 m, where he neglected seismic

40 attenuation on the basis of Bentley and Kohnen's results. However, as we show in the present work, attenuation in firn cannot be neglected, since the Q_P factor has values between 4 and 50 down to 40 m depth, thus inducing a strong energy loss and velocity dispersion near the surface.

Regarding the attenuation mechanisms, Bentley and Kohnen (1976) assume that their results are "consistent with damping in slightly contaminated ice by a combination of two mechanisms: molecular relaxation at temperatures colder than about -20

45 °C and grain boundary viscosity at warmer temperatures". However, they do not provide a physical predictive micro-structural model for attenuation. Grain boundary relaxation and melting theories based on the Arrhenius equation can be important at temperatures close to the melting point of ice. In the case of rocks such a model has been applied to describe seismic attenuation at the crust and mantle (Carcione et al., 2018).

Here we consider three attenuation mechanisms based on physical models. We show that wave-induced fluid flow generates

50 enough heat to explain the levels of intrinsic attenuation. This flow occurs at different spatial scales that can broadly be categorized as "macroscopic", "mesoscopic" and "microscopic". The macroscopic flow is the wavelength-scale equilibration occurring between the peaks and troughs of a P wave. This mechanism was first treated by Biot (1956) and is simply called "Biot loss". The microscopic flow occurs when a wave squeezes a porous medium having grain contacts and cracks, which respond with a greater fluid pressure than the main pore space resulting in a flow from crack to pores, named "squirt flow".

55 Finally, mesoscopic length scales are those much larger than grain sizes but smaller than wavelengths. Heterogeneity across these scales may be due to frame variations or to patches of different immiscible fluids. In our case, because of the seasonal alternation, the firn can be considered a finely layered medium consisting in the deposition of two porous media, one layer snow-like with high porosity and the other ice-like with low porosity (e.g., Greenhalgh and King, 1981). When a compressional wave squeezes such a medium, the effect is similar to squirt with the more compliant portions of the material responding with a

60 greater fluid pressure than the stiffer portions. Then, there is a flow of fluid capable of generating significant loss in the seismic

band. The fluid saturating the pores in this case is assumed to be fluidized snow, a mixture of snow particles and air (Mellor, 1974; Maeno and Nishimura, 1979; Nishimura, 1996). These three mechanisms are described in Pride et al. (2004), Carcione and Picotti (2006), and Carcione (2022).

In the present work, we infer the P- and S-wave quality factor vertical profiles of the firn layer of Whillans Ice Stream (WIS – West Antarctica), using the three-component seismic data recorded on the Subglacial Lake Whillans (SLW), during the active-source experiment described in Horgan et al. (2012) and Picotti et al. (2015). First, we describe the data, the attenuation rock-physics theories and the methodology to extract the Q factor from the seismograms. Then, we analyze the spectral content of the diving-wave first-breaks and compute the Q_P and Q_S factors using the frequency-shift technique. Finally, we fit the two vertical Q profiles using the presented rock-physics theories.

2 Seismic data

In the austral summer of 2010–2011, a comprehensive surface geophysics program surveyed a location on the WIS. The main target of the survey (Horgan et al., 2012; Christianson et al., 2012) was the seismic and radar characterization of the SLW (Fig. 1), an active subglacial lake that is the subject of a subglacial access program (Tulaczyk et al., 2014). Four active-source seismic profiles were acquired during this program: one profile parallel to the ice stream flow direction, following the long axis of the lake, and three transverse profiles across the lake (Fig. 1).

⟨⟨ Figure 1 ⟩⟩

Two types of surveys were undertaken: one to obtain the characteristics of the firn and another for the imaging (Horgan et al., 2012) and to define the anisotropy of the whole ice column (Picotti et al., 2015). For the analysis of the velocity profile within the firn, a shallow-refraction dataset was generated using stacked hammer blows onto a wooden body embedded in the snow. This experiment is located on the longitudinal profile, as shown in Fig. 1. The data were recorded on a 24-channel seismic system using georods spaced 20 m apart and consisting of five 40 Hz geophones wired in series (Voigt et al., 2013). The digital sample interval was 0.25 ms, and the maximum offset was 470 m, which is enough to define the velocity profile of the whole firn layer. To acquire the three components of the ground motion, the georods were rotated through the three mutually perpendicular axes. The horizontal longitudinal and transverse components are parallel and orthogonal to the profile, respectively. In the shallow-refraction survey, the trace spacing was increased with increasing offset to gain better resolution in the shallow part of the firn, which exhibits the strongest velocity gradient. The trace spacing is 1 m, 10 m and 20 m for offsets lower than 10 m, ranging between 10 and 290 m, and larger than 290 m, respectively. For the purposes of this work, generation and acquisition of S waves polarized in the orthogonal direction with respect to the seismic line (i.e., SH waves) is far better, because these are pure S waves, free of P-wave interferences. We also acquired the SV waves, polarized in the longitudinal vertical plane, but these signals are more affected by interferences from diving and multiple-refracted P-waves propagating

90 in firn. The obtained seismogram ensembles are shown in Fig. 2, where the P and SH diving-wave first breaks picked for the traveltime inversion and for the spectral analysis are indicated.

⟨⟨ Figure 2 ⟩⟩

All the other data, aimed at defining the imaging and the anisotropy of the whole ice column, were generated using 0.4 kg PETN (pentaerythritol tetranitrate) charges buried at 27 m depth using a hot-water drill. The data were recorded on a 48-channel seismic system, and the sensors consisted of alternating 28 Hz single vertical geophones and georods spaced 20 m apart. These data are described in more detail by Horgan et al. (2012) and Picotti et al. (2015).

3 Theory and Methodology

3.1 Theory overview

The theory of wave propagation in firn combines White's mesoscopic attenuation theory of interlayer flow (White et al., 1975; Carcione and Picotti, 2006; Carcione, 2022) and that of Biot/squirt flow (Gurevich et al., 2010; Carcione and Gurevich, 2011; Carcione, 2022). The first theory describes an equivalent viscoelastic medium of a stack of two thin alternating porous layers of thickness d_1 and d_2, such that the period of the stratification is $d = d_1 + d_2$. The theory gives the complex and frequency dependent stiffness E, equivalent to the P-wave modulus. The complex velocity is given in Appendix A. On the other hand, in the so-called Biot/squirt-flow model, there are two loss mechanisms, namely the Biot global-flow one (Biot, 1956) and local flow from fluid-filled micro-cracks (or grain contacts) to the pore space and back. Fig. 3 shows a sketch, where two sandstone grains in contact are shown.

⟨⟨ Figure 3 ⟩⟩

Gurevich et al. (2010) assumed that a compliant pore forms a disk shaped gap between two grains and its edge opens into a toroidal stiff pore, where R is the radius of the contact (or crack) and h is its thickness The model assumes that the material becomes stiffer when the fluid pressure does not have enough time to equilibrate between the stiff and compliant pores (grain contacts and main voids, respectively). To obtain the frequency dependency of the stiffness moduli, the complex velocity is given in Appendix B.

3.2 Phase velocity and quality factor

Denoting with 1 and 2 the subscripts corresponding to the mesoscopic and Biot/squirt-flow loss models, the global P-wave complex velocity and dissipation factor are

$$v_{pP} \approx v_{p2P} \tag{1}$$

4

115 and

$$\frac{1}{Q_{\mathrm{P}}} = \frac{1}{Q_1} + \frac{1}{Q_{2\mathrm{P}}},\tag{2}$$

respectively, where

$$v_{p2\mathrm{P}} = \left[\mathrm{Re}\left(\frac{1}{v_{2\mathrm{P}}}\right)\right]^{-1}\tag{3}$$

and

120 $$Q_1 = \frac{\mathrm{Re}(v_1^2)}{\mathrm{Im}(v_1^2)}, \quad Q_{2\mathrm{P}} = \frac{\mathrm{Re}(v_{2\mathrm{P}}^2)}{\mathrm{Im}(v_{2\mathrm{P}}^2)}.\tag{4}$$

Since the dominant mechanism is the Biot/squirt-flow one, we assume as a first approximation that the P-wave phase velocity is that of this loss mechanism. Alternatively, the phase velocity (1), $v_{p\mathrm{P}}(\omega)$, can be obtained from $Q_P(\omega)$ by using the Kramers-Kronig relations as given in Eq. 8 of Carcione et al. (2020) (see also Eq. (2.141) of Carcione, 2022).

Equation (2) can be demonstrated if we consider that the decay factor along a distance r of a plane wave, due to the effect

125 of the two attenuation mechanisms, is

$$\exp(-\alpha_1 r)\exp(-\alpha_{2\mathrm{P}} r),\tag{5}$$

where α are attenuation factors given by

$$\alpha_1 = \frac{\pi f}{v_{p1}Q_1}, \quad \alpha_{2\mathrm{P}} = \frac{\pi f}{v_{p2\mathrm{P}}Q_{2\mathrm{P}}},\tag{6}$$

for low-loss media, v_{p1} is the mesoscopic-loss phase velocity and f is the frequency (see Eq. (2.129) in Carcione (2022)).

130 Substituting (6) into (5), we obtain

$$\exp\left(-\frac{\pi f r}{v_{p\mathrm{P}}Q_P}\right),\tag{7}$$

where we have assumed $v_{p1} \approx v_{p2\mathrm{P}}$.

On the other hand, the properties of the S wave is solely described by the Biot/squirt-flow model, such that

$$v_{p\mathrm{S}} = \left[\mathrm{Re}\left(\frac{1}{v_{2\mathrm{S}}}\right)\right]^{-1}\tag{8}$$

135 and

$$Q_{\mathrm{S}} = \frac{\mathrm{Re}(v_{2\mathrm{S}}^2)}{\mathrm{Im}(v_{2\mathrm{S}}^2)}.\tag{9}$$

3.3 Estimation of the quality factor

To estimate the quality factor from the seismograms we adopted the frequency-shift method (e.g., Quan and Harris, 1997; Picotti et al., 2007). Let $S(f)$ and $R(f)$ be the amplitude quasi-Gaussian spectra observed at the source and at a receiver,

The Cryosphere
Discussions

140 respectively, located at a mutual distance d in an homogeneous and isotropic medium. The frequency-shift approach is based on the property that, as the wave propagates through the medium, the high frequency part of the spectrum decreases faster than the low frequency part (Quan and Harris, 1997). This effect may be quantified by measuring the resulting downshift $\Delta f = f_S - f_R$, where f_S and f_R are the frequency centroids of $S(f)$ and $R(f)$, respectively. Then, if we approximate the spectrum $S(f)$ by a Gaussian with variance σ_S^2, we have

145
$$Q = \frac{\pi d \sigma_S^2}{v \Delta f} = \frac{\pi \Delta t \sigma_S^2}{\Delta f}, \tag{10}$$

where v is the velocity (P- or S-wave velocity), and Δt is the traveltime. Although this method is applicable under the hypothesis of constant-Q in the bandwidth of interest (Dasgupta and Clark, 1998; Quan and Harris, 1997), it can be applied with good reliability also to frequency-dependent Q media. For example, Picotti et al. (2007) estimated the frequency-dependent Q from numerically simulated seismograms by using the spectral-ratio and frequency-shift methods, finding values in very good agreement with the synthetic theoretical models. Moreover, they found that the classical spectral-ratio method is more
150 sensitive to this problem, resulting in noticeable departures of the logarithm of the spectral ratio from the linear trend. On the other hand, the frequency-shift method is less sensitive to this problem when the spectrum of the signal is Gaussian, because generally the variation of the quality factor is weak in the seismic frequency band, and becomes important only at very high and low frequencies. In these zones, the amplitude of the Gaussian signal is very low, resulting in small contributions in the
155 integrals for the computation of variances and frequency centroids.

In the more general case of inhomogeneous media, the frequency shift along a raypath can be expressed as

$$\Delta f = \sigma_S^2 \int_{ray} \alpha_0 dl, \tag{11}$$

(Quan and Harris, 1997), where the integral is taken along the raypath and $\alpha_0 = \pi/Qv$ is the attenuation factor, i.e., the attenuation coefficient is linearly proportional to frequency and defined as $\alpha = \alpha_0 f$. To infer the vertical Q profile of firn, we
160 consider the whole firn column as a sequence of homogeneous-Q layers. The Q of each individual layer is obtained adopting a layer-stripping method that considers the cumulative attenuation of all the overlying layers and exploits the monotonically increase of the firn's P- and S-wave velocities. The layer-stripping method is a well established technique both in traveltime and attenuation tomography (e.g., Yilmaz, 2001; Böhm et al., 2006; Rossi et al., 2007). The P- and S-wave velocity fields (Fig. 4a) were previously computed in Picotti et al. (2015) by the traveltime inversion of first arrivals, following the method of
165 Herglotz and Wiechert (Herglotz, 1907; Wiechert, 1910; Nowack, 1990). This technique, applied for the first time to Antarctic seismic data by Kirchner and Bentley (1979), calculates the velocity-depth function from traveltime-offset picked first-breaks. It is well suited to situations where the velocity increases monotonically with depth and for this reason it was successfully applied to firn by several authors (e.g., King and Jarvis, 2007). The resulting diving-wave paths in the velocity gradient (Fig. 4b) are obtained using an optimized ray-tracing algorithm based on the shooting method, described in Picotti et al. (2015).

⟨⟨ Figure 4 ⟩⟩

170   Let's consider a layer N in this succession, and assume the value of Q in the overlying $N-1$ layers to be already known. In our plane-layered model, the depth of each layer coincides with the depth of maximum penetration of each ray at increasing offsets. The ray corresponding to this layer reaches a receiver at the surface, whose recorded first-break frequency centroid is f_R. Under our hypothesis, and accordingly with equation (11), the total frequency-shift occurred in the overlying $N-1$ layers is

175
$$\Delta f_{N-1} = 2 \sum_{i=1}^{N-1} \frac{\pi d_i \sigma_S^2}{v_i Q_i}, \tag{12}$$

where d_i are the lengths of the ray segments in each layer, and the factor 2 accounts for both the downgoing and the upgoing wave. Then, the quality factor of the layer N is simply obtained by equation (10), where $d = d_N$, $v = v_N$ and the frequency-shift in the layer N is given by $\Delta f = \Delta f_N = f_S - f_R - \Delta f_{N-1}$.

The layer-stripping method requires that the quality factor of the shallowest layer is known a priori. Moreover, the frequency
180   centroid f_S and variance σ_S of the source must be known as well. These two values can be determined using the first-breaks recorded by the receivers placed close to the source. To this purpose, it is necessary that the acquisition geometry is properly set to have a sufficient number of traces at very short offsets. Then, particular care must be devoted to acquire the first-breaks with a high-quality of the signal, e.g., the wavelets must be free of interference effects and their amplitudes not clipped. If such type of signals are available, the following considerations allow to compute the above required spectral properties. It is convenient
185   in this case to use equation (10) to obtain the difference in frequency content of propagating wavelets at different receivers. We consider the closest available signal to the source as reference wavelet, to be compared with the first breaks recorded at increasing offsets. In other words, we compare the spectrum $R_1(f)$ of the reference wavelet to that of another wavelet $R_2(f)$, which propagated for an additional traveltime Δt in the same shallow layer. If the traces are sufficiently closer to each other and to the source, it is possible to characterize the the quality factor of the uppermost layer as average of all calculated values,
190   and the variance σ_S can be approximated to that of the reference wavelet. Finally, the dominant frequency of the source f_S follows from equation (10) by using the reference first-break traveltime.

4   Results

4.1   Quality factor vertical profiling

As previously described, a requirement for the layer-stripping technique is the knowledge of the quality factor of the shallowest
195   layer, as well as the dominant frequency and variance of the source. We determined these properties, both for P and S waves, by using the first breaks recorded at short offsets.

Fig. 5 shows the wavelets (a) and the corresponding spectra (b) of the P-wave first breaks recorded between 7 and 10 m.

⟨⟨ Figure 5 ⟩⟩

Unfortunately, the first breaks recorded at offsets lower than 7 m are contaminated by the SV waves, and the amplitudes very close to the source are clipped. Taking the signal recorded at 7 m offset as reference wavelet, we computed the frequency shifts

200 and using equation (10) we estimated the average P-wave quality factor of the shallowest layer to be $Q_P = 4.1\pm2.6$. Calculating the maximum penetration depth of the ray emerging at 10 m offset, we estimated the thickness of this layer to be about 2.7 m thick. Moreover, the estimated source dominant frequency and variance are f_S= 574 Hz and σ_S= 171 Hz, respectively. Fig. 6 shows the wavelets (a) and the corresponding spectra (b) of the S-wave first breaks recorded between 2 and 6 m.

⟨⟨ Figure 6 ⟩⟩

Because of the amplitudes of the first break recorded at 1 m offset are clipped, the near trace cannot be used. Taking the

205 signal recorded at 2 m offset as reference wavelet, we computed the frequency shifts and using equation (10) we estimated the average S-wave quality factor of the shallowest layer to be $Q_S = 1.9\pm0.5$. Considering the very short offsets, the thickness of this layer is set equal to the wavelength, which is very short because of the low velocity and high frequency. The estimated source dominant frequency and variance are f_S= 496 Hz and σ_S= 146 Hz, respectively. Therefore, the estimated thickness of the shallowest layer is of about 0.2 m.

210 Fig. 7 shows the wavelet frequency centroids of the P- and S-wave diving first breaks. Both curves show a rapid decrease in the dominant frequency of the signal versus offset, except an increase in frequency for the P-waves between 10 and 30 m offset, which is an effect due to the diving waves travelling in that strong velocity-Q gradient.

⟨⟨ Figure 7 ⟩⟩

These two frequency datasets, as well as the spectral source characteristics and Q_P and Q_S of the shallowest layer, are used to compute the P- and S-wave quality factor profiles of the whole firn column using the layer-stripping procedure. As described

215 in the previus section the P- and S-wave velocity fields (Fig. 4a) were previously computed in Picotti et al. (2015) by the traveltime inversion of first arrivals, following the method of Herglotz and Wiechert (Herglotz, 1907; Wiechert, 1910; Nowack, 1990). The maximum P- and S-wave velocities, verified using the refracted first arrivals at the far offsets on the seismograms acquired using the explosive source, are 3864±15 m/s and 1947±20 m/s at 60±5 m depth, respectively (Picotti et al., 2015). The errors increase to about ±40 m/s at short offsets, because of the very steep gradient close to the surface. Fig. 8 and 9

220 display the resulting Q_P and Q_S profiles for the whole firn column, from the surface to the ice, together with the dominant frequency computed at the maximum penetration depth of each diving raypath.

⟨⟨ Figure 8 ⟩⟩

⟨⟨ Figure 9 ⟩⟩

The first plot (Fig. 8) shows a gradual increase of Q_P from the previously computed minimum value of 4.1±2.6 close to the surface, to a value of 100±40 at about 50 m depth. Then, it increases sharply to over 290±160 at about 58 m depth. The second plot (Fig. 9) exhibit a moderate increase of Q_S, from the previously computed minimum value of 1.9±0.5 close to the surface, to an average maximum value of about 280±130, which remains almost constant at depths larger than 35 m.

Since the offset range is not sufficient to appreciate where the Q_P factor stabilizes at the maximum value in the ice, we used the dataset acquired with the explosive charges placed at 27 m depth, to analyze the refracted first breaks recorded at very long offsets. Fig. 10 shows the wavelets (b) and the corresponding spectra (c), together with a reference wavelet recorded at 670 m offset (a,c). All these signals travel along very similar raypaths in the firn, while their paths in the underlying ice have different length. Following the same principle adopted for the computation of the Q factor in the shallowest layer, we compare the spectrum of the reference wavelet to those of other wavelets that propagated for additional traveltimes in the deep ice. Since these paths in the ice are very long, from 1120 to 1240 m, it is possible to appreciate a difference in the spectrum centroids and to compute the quality factors with a sufficient reliability. In this case, the average ice P-wave quality factor is of $Q_P = 378±108$ at 60±5 m depth, where the measured average temperature is approximately -24°C (Engelhardt and Kamb, 1993).

⟨⟨ Figure 10 ⟩⟩

4.2 Modeling of firn seismic properties

Firn is assumed to be a deposition of two porous media, one layer snow-like with high porosity and the other ice-like with low porosity. The grains (ice) have the properties $K_s = 10$ GPa, $\mu_s = 5$ GPa (shear modulus) and $\rho_s = 917$ kg/m^3 in both layers. The fluid saturating the pores is assumed to be fluidized snow, which is defined as a mixture of snow particles and air, like powder, having zero rigidity modulus. The properties of this material have been investigated by Mellor (1974), Maeno and Nishimura (1979) and Nishimura (1996). We consider $K_f = 571$ MPa, $\rho_f = 200$ kg/m^3 and $\eta = 0.1$ Pa s.

For each layer, the dry-rock bulk modulus which best fits the data of Johnson (1982) is

$$K_m = K_s(1-\phi)^{30.85/(7.76-\phi)}. \tag{13}$$

The dry-rock shear modulus is

$$\mu = \frac{3}{2}\frac{1-2\nu}{1+\nu}K_m, \quad \nu = 0.38 - 0.36\phi, \tag{14}$$

where ν is the Poisson ratio.

The permeability is

$$\kappa = \frac{C}{\rho_s^2} \cdot \frac{\phi^3}{(1-\phi)^2} \tag{15}$$

The Cryosphere
Discussions

EGU

(Sidler, 2015; Gurevich and Carcione, 2023), where C is a constant. The local period of the stratification is $d = 0.1$ m with p_1 = 0.5.

250   The density profile as a function of depth depth is obtained by using the following empirical relationship

$$\rho(z) = 0.917 \left[1 + \left(\frac{V_{P,ice} - V_P(z)}{2250} \right)^{1.22} \right]^{-1}, \tag{16}$$

Kohnen (1972), where $V_P(z)$ is the vertical P-wave velocity displayed in Fig. 4 (a), and $V_{P,ice} = 3864$ m/s is the ice P-wave velocity, which we assume equal to the maximum computed P-wave velocity.

The porosity obtained from the experimental density (16) is

$$\phi(z) = \frac{\rho_s - \rho(z)}{\rho_s - \rho_f}. \tag{17}$$

255   Fig. 11 shows the experimental density (a) and porosity (b) as a function of depth. These quantities increase monotonically versus depth mainly due to compaction.

$\langle\langle$ Figure 11 $\rangle\rangle$

For the mesoscopic-loss model, we assume $\phi_1(z) \approx \phi(z)$, $p_1 = p_2 = 0.5$ and $\phi_2 = \gamma\phi_1$, where γ is small, i.e., layer 2 has a much lower porosity than layer 1. Here we assume $\gamma = 0.1$.

260   On the other hand, the squirt-flow model has the following values of the parameters: $h/R = 0.015$, $\phi_c = 0.0002$, $K_h = 1.38K_m$, where K_m is the bulk modulus with the grain contacts and cracks open, $C = 0.012$ kg^2/m^4, and we consider that the porosity ϕ is obtained from the experimental velocities and density as given by equation (17). The attenuation is due to the softer layer with much higher porosity, since the cracks are open and the global-flow loss (Biot) mechanism is effective. The contribution of the stiff layer is negligible.

265   Fig. 12 shows the P- and S-wave velocity and dissipation factor as a function of frequency close to the surface, where $\phi_1 = 0.744$, $\phi_2 = 0.0744$, and the solid and fluid properties of the two layers are the same. We can see that the dominant mechanism is the Biot (global-flow) one (Biot, 1956), with a strong peak and velocity dispersion. The squirt-flow peak is weaker and located at lower frequencies, while the mesoscopic loss contributes only to the P wave. The P- and S-wave dissipation peaks occur at a frequency of approximately 282 Hz. On the other hand, the model predicts that below a given depth (from 40 to 50

270   m) the squirt-flow loss predominates over the Biot global one.

$\langle\langle$ Figure 12 $\rangle\rangle$

Let us now study the dependence of attenuation as a function of depth. We consider a frequency of 282 Hz, corresponding to the dissipation peaks in Fig. 12. Fig. 13a shows the comparison between the experimental and theoretical quality factor profiles

as a function of depth, while Fig. 13b shows the Q_P and Q_S experimental errors. As expected, the experimental errors increase with increasing quality factor, in agreement with the fact that the attenuation effects weakens with increasing Q, and can be

275 observed with high accuracy only over large distances. The differences between the theoretical quality factor models and the profiled Q are within the experimental errors for all the firn column.

$\langle\langle$ Figure 13 $\rangle\rangle$

5 Conclusions

A physical explanation of the seismic attenuation (quality factor) in polar firn, as well as that of the underlying ice, is essential to obtain information about the ice cap and deeper geological formations. In particular, the proposed model is useful to perform

280 data processing and amplitude-versus-offset (AVO) inversions to extract the petrophysical basal properties from multichannel active-source seismic data. In this work we estimate the P- and S-wave attenuation profiles in the firn of Whillans Ice Stream (West Antarctica) from spectral analysis of diving-wave first-breaks of three-component active-source seismic data. The resulting experimental quality factors range from values as low as 5 at the surface to approximately 300 at about 60 m depth. Then, the P-wave quality factor further increases until a maximum value of about 378 in the underlying ice. The model of

285 wave propagation in firn combines White's mesoscopic attenuation theory of interlayer flow and that of Biot/squirt flow, and the fluid saturating the pores is assumed to be fluidized snow. It is found that the dominant attenuation mechanism is the Biot global flow one, with the theory showing a good agreement with the experimental values for the whole firn column. The model also predicts that below a given depth (from 40 to 50 m) the squirt-flow loss predominates over the Biot global one.

Data availability. The data presented in this work is available through the following previous publications: Horgan et al. (2012) and Picotti

290 et al. (2015).

Appendix A: Mesoscopic-loss model

The P-wave modulus is (White et al., 1975; Carcione, 2022)

$$E = \left[\frac{1}{E_0} + \frac{2(r_2 - r_1)^2}{i\omega(d_1 + d_2)(I_1 + I_2)} \right]^{-1}. \tag{A1}$$

where

295 $$E_0 = \left(\frac{p_1}{E_{G_1}} + \frac{p_2}{E_{G_2}} \right)^{-1}, \tag{A2}$$

with $p_l = d_l/(d_1 + d_2)$, $l = 1, 2$,

$$r = \frac{\alpha M}{E_G} \tag{A3}$$

$$I = \frac{\eta}{\kappa a} \coth\left(\frac{ad}{2}\right), \quad a = \sqrt{\frac{\mathrm{i}\omega\eta E_G}{\kappa M E_m}}, \tag{A4}$$

300   for each single layer, ω is the angular frequency and $\mathrm{i} = \sqrt{-1}$.

Moreover, for each layer

$$E_m = K_m + \frac{4}{3}\mu \tag{A5}$$

is the dry-rock P-wave modulus, being K_m and μ the respective bulk and shear moduli,

$$E_G = E_m + \alpha^2 M \tag{A6}$$

305   is Gassmann's P-wave modulus,

$$K_G = K_m + \alpha^2 M, \tag{A7}$$

is Gassmann's bulk modulus,

$$\alpha = 1 - \frac{K_m}{K_s}, \quad M = \left(\frac{\alpha - \phi}{K_s} + \frac{\phi}{K_f}\right)^{-1}, \tag{A8}$$

where ϕ, K_s and K_f denote the porosity, and the bulk moduli of the grains and saturant fluid, respectively. The coefficient α

310   is known as the effective stress coefficient of the bulk material. Finally, η is the fluid viscosity and κ is the frame permeability.

Let ρ_s and ρ_f denote the mass densities of the grains and fluid, respectively, and let

$$\rho = (1 - \phi)\rho_s + \phi\rho_f \tag{A9}$$

denote the mass density of the bulk material.

The complex velocity is

315    $$v_1 = \sqrt{\frac{E}{\rho}}. \tag{A10}$$

This model considers only the P-wave attenuation, since the shear modulus μ is real.

Appendix B: Biot/squirt-flow model

The poroelastic coefficients are the Gassmann bulk and shear moduli,

$$K_G = K_m + \alpha(K_m)^2 M(K_m) \quad \text{and} \quad \mu_G = \mu_m \tag{B1}$$

320   where

$$\alpha(K_m) = 1 - \frac{K_m}{K_s} \quad \text{and} \quad M(K_m) = \frac{K_s}{1 - \phi - K_m/K_s + \phi K_s/K_f}, \tag{B2}$$

ϕ is the porosity, K_m and μ_m are the bulk and shear moduli of the drained matrix, and K_s and K_f are the solid and fluid bulk moduli, respectively. We explicitly indicate the functional form of α and M on K_m, since we shall replace this modulus by a modified matrix (or frame) complex modulus K, which includes the squirt-flow mechanism. In the same manner, μ_m will be
325   replaced by μ. The new moduli are complex-valued and frequency-dependent.

In the Biot/squirt-flow model, the bulk and shear moduli of the saturated rock at low frequencies are given by Gassmann's equations,

$$K_G = \overline{K} + \alpha^2(\overline{K})M(\overline{K}) \quad \text{and} \quad \mu_G = \overline{\mu}, \tag{B3}$$

where $\overline{K}$ and $\overline{\mu}$ are the bulk and shear moduli of the modified frame including the un-relaxation due to the presence of the
330   squirt-flow mechanism, and α and M are given by equation B2 substituting K_m with K. For simplicity, we keep the same notation for the Gassmann moduli, but now they are complex-valued and frequency-dependent.

Gurevich et al. (2010) obtained the modified dry moduli in the following form

$$\frac{1}{\overline{K}} = \frac{1}{K_h} + \left[\left(\frac{1}{K_m} - \frac{1}{K_h} \right)^{-1} + \left(\frac{1}{K_f^*} - \frac{1}{K_s} \right)^{-1} \phi_c^{-1} \right]^{-1}, \tag{B4}$$

$$\frac{1}{\overline{\mu}} = \frac{1}{\mu_m} - \frac{4}{15} \left(\frac{1}{K_m} - \frac{1}{\overline{K}} \right),$$

where K_m and μ_m are the dry-rock bulk and shear moduli at the confining pressure p_c, K_h is the dry-rock bulk modulus at a
335   confining pressure where all the compliant pores are closed, i.e., an hypothetical rock without the soft porosity, and ϕ_c is the compliant porosity. This is so small – nearly 0.001 for most rocks – that the total porosity ϕ can be assumed to be equal to the stiff porosity. The key quantity in equations B4 is the effective bulk modulus of the fluid saturating the soft pores:

$$K_f^* = \left[1 - \frac{2J_1(kR)}{kRJ_0(kR)} \right] K_f, \quad k = \frac{2}{h} \sqrt{-\frac{3i\omega\eta}{K_f}} = \frac{1}{R} \sqrt{\frac{-8K_f^*}{K_f}}, \tag{B5}$$

where J_0 and J_1 are Bessel functions.
340   The complex velocities of the P and S waves are

$$v_{2P} = \sqrt{\frac{\overline{K} + 4\overline{\mu}/3}{\rho}} \tag{B6}$$

and

$$v_{2S} = \sqrt{\frac{\overline{\mu}}{\rho}}, \tag{B7}$$

respectively.

References

Albert, D.G.: Theoretical modeling of seismic noise propagation in firn at the South Pole, Antarctica, Geophys. Res. Lett., 25(23),
355   4257–4260, 1998.

van den Broeke, M. : Depth and Density of the Antarctic Firn Layer. Arctic, Antarctic, and Alpine Research, 40(2), 432–438,
       http://www.jstor.org/stable/20181806, 2008.

Bentley, C. R. and Kohnen, H.: Seismic refraction measurements of internal friction in Antarctic ice, J. Geophys. Res., 81, 1519–1526, 1976.

360

Biot, M. A.: Theory of propagation of elastic waves in a fluid-saturated porous solid. I. Low frequency range, J. Acoust. Soc. Am., 28,
       168–178, 1956.

Böhm, G., Accaino, F., Rossi, G., Tinivella, U.: Tomographic joint inversion of first arrivals in a real case from Saudi Arabia, Geophysical
365   Prospecting, 54, 721 – 730, https://doi.org/10.1111/j.1365-2478.2006.00563.x., 2006.

Carcione, J. M.: Wave Fields in Real Media. Theory and numerical simulation of wave propagation in anisotropic, anelastic, porous and
       electromagnetic media, Elsevier (Fourth edition, extended and revised), 2022.

370   Carcione, J. M., Gei, D., Picotti, S., Botelho, M.A.B.: On the instantaneous frequency and quality factor. Geophysical Journal International,
       227(2), 735–745, https://doi.org/10.1093/gji/ggab250, 2021.

Carcione, J. M., Gei, D., Santos, J. E., Fu, L.-Y. and Ba, J.: Canonical analytical solutions of wave-induced thermoelastic attenuation,
       Geophys. J. Int., 221, 835–842, 2020.

375

Carcione, J. M. and Gurevich, B.: Differential form and numerical implementation of Biot's poroelasticity equations with squirt dissipation,
       Geophysics, 76, N55–N64, 2011.

Carcione, J. M., Poletto, F., Farina, B. and Bellezza, C.: 3D seismic modeling in geothermal reservoirs with a distribution of steam patch
380   sizes, permeabilities and saturations, including ductility of the rock frame, Physics of the Earth and Planetary Interiors, 279, 67–78, 2018.

Carcione, J. M. and Picotti, S.: P-Wave seismic attenuation by slow-wave diffusion: Effects of inhomogeneous rock properties, Geophysics,
       71, O1-O8, 2006.

385   Christianson, K., Jacobel, R.W., Horgan, H.J., Anandakrishnan, S. and Alley, R.B.: Subglacial Lake Whillans – Ice-penetrating radar and
       GPS observations of a shallow active reservoir beneath a West Antarctic ice stream, Earth and Planetary Science Letters, 331 - 332, 237 -
       245, 2012.

Clee, T. E., Savage, J. C. and Neave, K. G. : Internal friction in ice near its melting point, J. Geophys. Res., 74(4), 973–980,
390   https://doi.org/10.1029/JB074i004p00973, 1969.

Dasgupta, R. and Clark, R. A.: Estimation of Q from surface seismic reflection data: Geophysics, 63, 6,2120–2128, 1998.

Engelhardt, H. and Kamb, B. : Vertical temperature profile of ice stream B, Antarct. J. Rev., 28, 63–66, 1993.
395

Greenhalgh, S. A. and King, D. W.: Curved raypath interpretation of seismic refraction data, Geophysical Prospecting, 29(6), 853-882, 1981.

Gurevich, B. and Carcione, J. M.: Attenuation and dispersion in fluid-saturated porous rocks: Mechanisms and models, SEG publication,
         26, 2023.
400

Gurevich, B., Makarynska, D., de Paula, O. and Pervukhina, M.: A simple model for squirt-flow dispersion and attenuation in fluid-saturated
         granular rocks, Geophysics, 75, N109–N120, 2010.

Gusmeroli, A., Clark, R. A., Murray, T., Booth, A. D., Kulessa, B. and Barrett, B. E.: Seismic wave attenuation in the uppermost glacier ice
405   of Storglaciären, Sweden, Journal of Glaciology, 56(196), 249–256, https://doi.org/10.3189/002214310791968485, 2010.

Herglotz, G.: Über das Benndorfsche Problem der Fortpflanzungsgeschwindigkeit der Erdbebenstrahlen, Physikal, Zeitschr. für Geophys.,
         8, 145–147, 1907.

Herron, M.M. and Langway, C.C.: Firn densification, an empirical model, Journal of Glaciology, 25, 373–385, 1980.
410

Horgan, H.J., Anandakrishnan, S., Christianson, K., Jacobel, R.W., Alley, R. B., Heeszel, D. S., Picotti, S. and Jacob I. W.: Subglacial Lake
         Whillans – Seismic observations of a shallow active reservoir beneath a West Antarctic ice stream, Earth and Planetary Science Letters,
         331–332, 201–209, 2012.
415

Johnson, J. B.: On the application of Biot's theory to acoustic wave propagation in snow, Cold Regions Science and Technology, 6, 49–60,
         1982.

King, E. C. and Jarvis, E. P.: Use of shear waves to measure Poisson's ratio in polar firn, Journal of Environmental and Engineering
420   Geophysics, 12(1), 15–21, 2007.

Kirchner, J.F. and Bentley, C.R.: Seismic short refraction studies on the Ross Ice Shelf, Antarctica, Journal of Glaciology, 24(90), 313–319,
         1979.

425 Kohnen, H.: On the relation between seismic velocities and density in firn and ice, Z. Geophys, 38, 925–935, 1972.

Kuroiwa, D. : Internal friction of ice. III : The internal friction of natural glacier ice. Contributions from the Institute of Low Temperature Science, 18, 49–62, 1964.

430 Maeno, N. and Nishimura, K.: Fluidization of snow, Cold Reg. Sci. Technol., 1, 109–120, 1979.

Mellor, M.: A review of basic snow mechanics, U.S. Army Cold Regions Research and Engineering Laboratory, - Snow mechanics, 1974.

Nishimura, K.: Viscosity of fluidized snow, Cold Regions Science and Technology, 24, 117–127, 1996.

435

Nowack, R. L.: Tomography and the Herglotz-Wiechert inverse formulation, Pure and Applied Geophysics, 133, 305–315, 1990.

Oraschewski, F. M. and Grinsted, A.: Modeling enhanced firn densification due to strain softening, The Cryosphere, 16, 2683–2700, https://doi.org/10.5194/tc-16-2683-2022, 2022.

440

Peters, L. E., Anandakrishnan, S., Alley, R. B. and Voigt, D. E. : Seismic attenuation in glacial ice: A proxy for englacial temperature, J. Geophys. Res., 117, F02008, https://doi.org/10.1029/2011JF002201D, 2012.

Picotti, S., Carcione, J. M., Rubino, J. G. and Santos, J. E.: P-wave seismic attenuation by slow-wave diffusion: Numerical experiments in partially saturated rocks, Geophysics, 72 (4), N11–N21, https://doi.org/10.1190/1.2740666, 2007.

445

Pride, S. R., Berryman, J. G. and Harris, J. M.: Seismic attenuation due to wave-induced flow, J. Geophys. Res., 109, B01201, 2004.

Quan, Y. and Harris, J. M.: Seismic attenuation tomography using the frequency shift method, Geophysics, 62, 895–905, 1997.

450 Rossi, G., Gei, D., Böhm, G., Madrussani, G., Carcione, J. M.: Attenuation tomography: An application to gas-hydrate and free-gas detection. Geophysical Prospecting, 55, 655–669, https://doi.org/10.1111/j.1365-2478.2007.00646.x, 2007.

Sidler, R.:A porosity-based Biot model for acoustic waves in snow, Journal of Glaciology, 61, 789–797, 2015.

455 Tulaczyk, S., Mikucki, J., Siegfried, M., Priscu, J., Barcheck, C., Beem, L. and The Wissard Science Team: WISSARD at Subglacial Lake Whillans, West Antarctica: Scientific operations and initial observations. Annals of Glaciology, 55(65), 51–58. doi:10.3189/2014AoG65A009, 2014.

Voigt, D.E., Peters, L. E and Anandakrishnan, S.: 'Georods': The development of a four-element geophone for improved seismic imaging 460 of glaciers and ice sheets, Annals of Glaciology, 54(64), 142–148, 2013.

White, J. E., Mikhaylova, N. G. and Lyakhovitskiy, F. M.: Low-frequency seismic waves in fluid saturated layered rocks, Physics of the Solid Earth, 11, 654–659, 1975.

465   Wiechert, E.: Bestimmung des weges von erdbebenwellen, I. Theoretisches. Phys. Z., 11, 294-304, 1910.

Wilkinson, D. S.: A pressure-sintering model for the densification of polar firn and glacier ice, Journal of Glaciology, 34, 40–45, 1988.

Yilmaz, O.: Seismic data analysis: processing, inversion and interpretation of seismic data, SEG Series: Investigation in Geophysics, Tulsa,
470   2001.
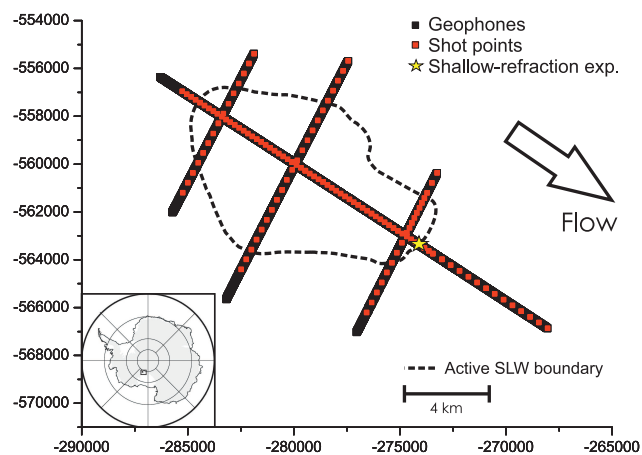
Figure 1. Map showing the location of SLW and the survey profile geometry. The location of the shallow-refraction experiment is indicated (modified from Picotti et al., 2015). Polar stereographic projection with true scale at -71°.
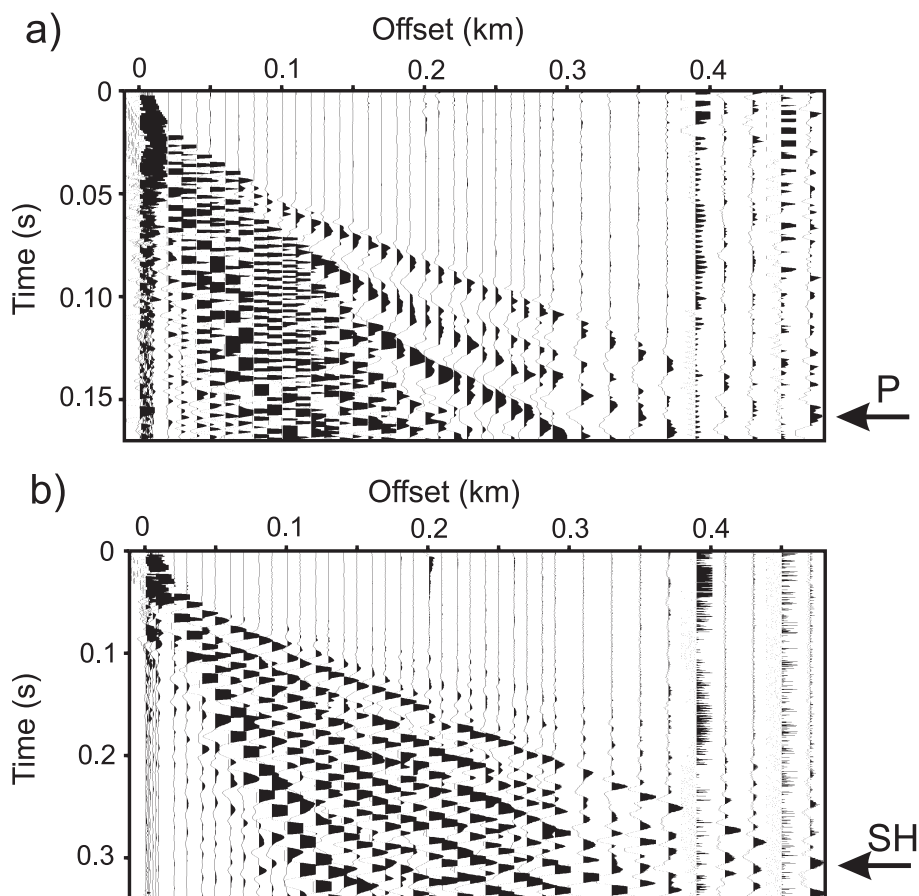
Figure 2. Hammer shallow-refraction seismograms as recorded by the georods along the longitudinal profile (modified from Picotti et al., 2015). The vertical component is shown in (a), while the horizontal transverse component is shown in (b), respectively. To acquire the three components, the georods were rotated through the three mutually perpendicular axes. The P and SH diving-wave first breaks are indicated.
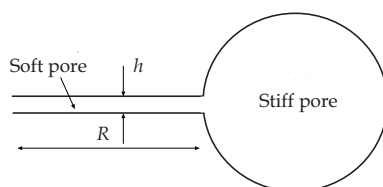
Figure 3. Sketch of the squirt-flow model, where two sandstone grains in contact are shown. The soft pores are the grain contacts and the stiff pores constitute the main porosity. The quantity R is the radius of the disk-shaped soft pore (half disk is represented in the plot).

a)

b)
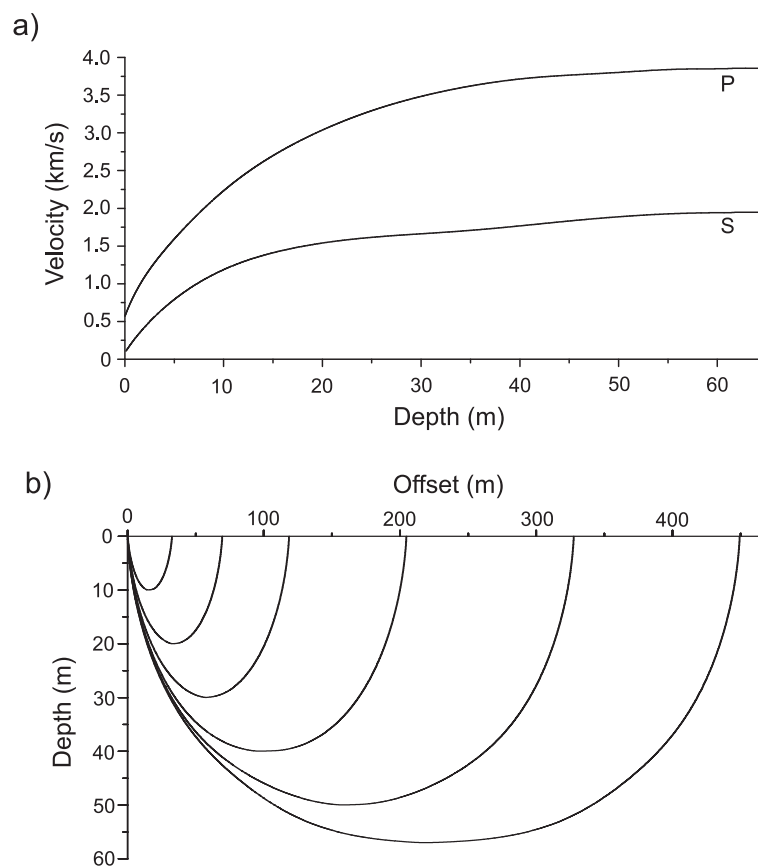
Figure 4. P-wave and S-wave velocity profiles versus depth obtained by Picotti et al. (2015) using the Hergloz-Wiechert traveltime inversion method (a) and P-wave diving waves corresponding to certain picked first-breaks (b).
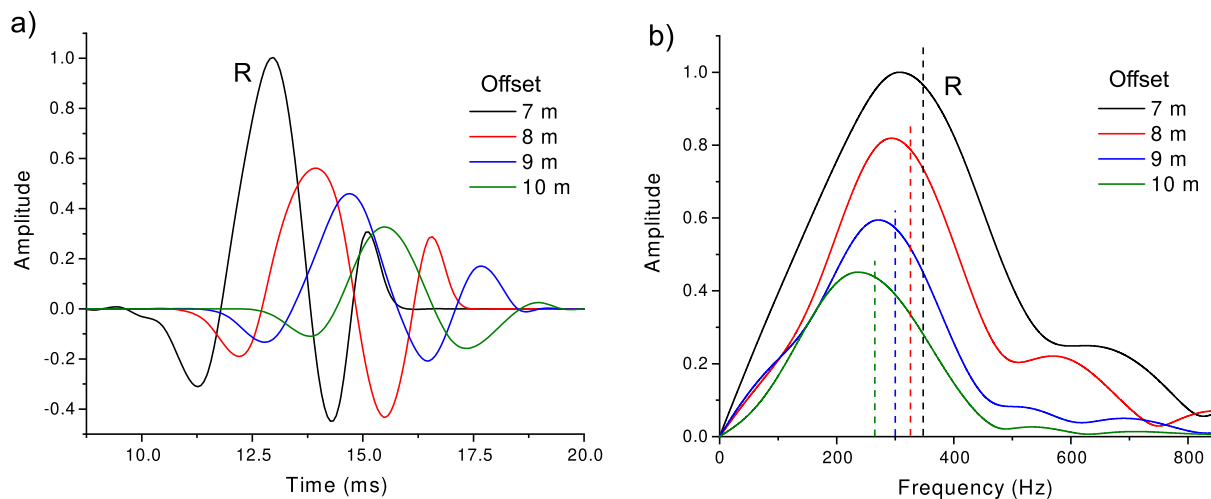
Figure 5. Wavelets (a) and corresponding spectra (b) of the P-wave first breaks recorded between 7 and 10 m. The label R indicates the reference signal recorded at 7 m offset, while the vertical dashed lines indicate the frequency centroids.
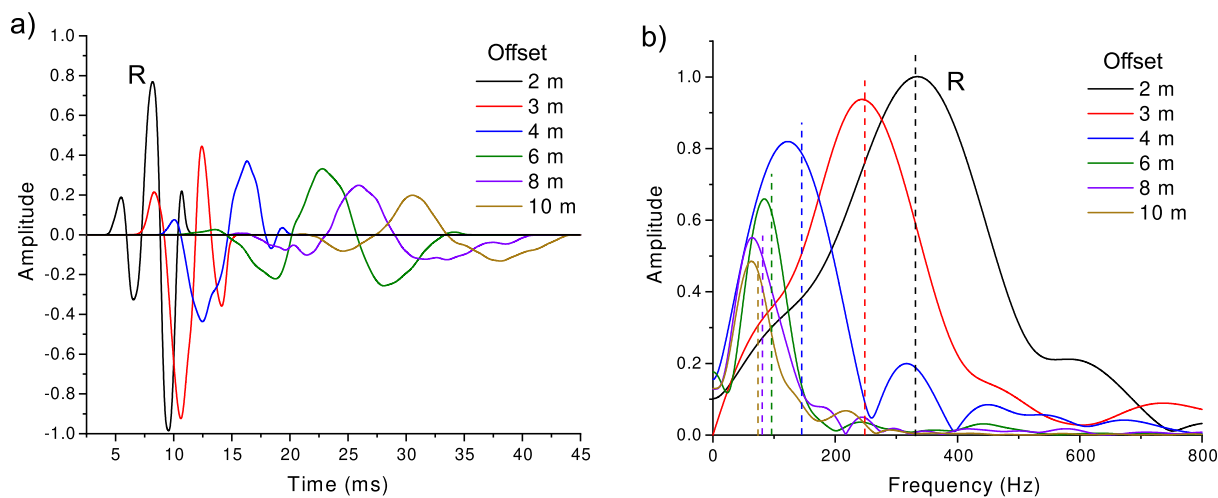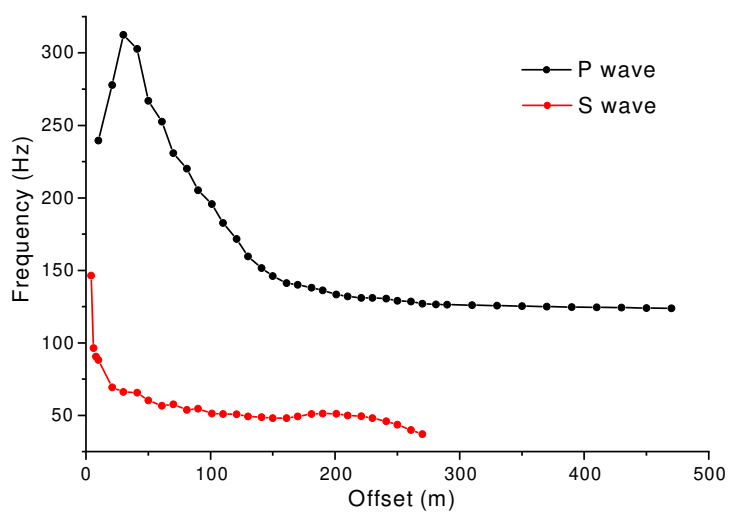

Figure 6. Wavelets (a) and corresponding spectra (b) of the S-wave first breaks recorded between 2 and 10 m. The label R indicates the reference signal recorded at 2 m offset, while the vertical dashed lines indicate the frequency centroids.

Figure 7. Dominant frequency of the P-wave (a) and S-wave (b) diving first-breaks versus offset.
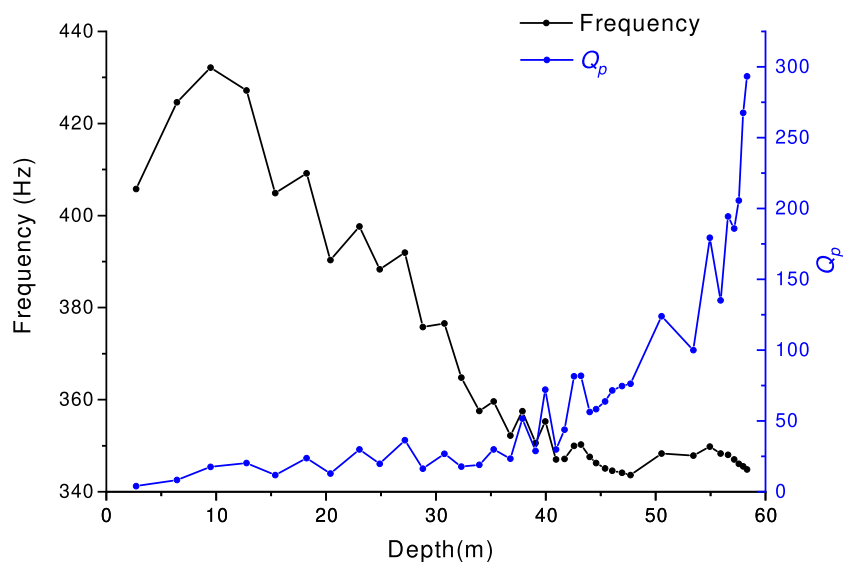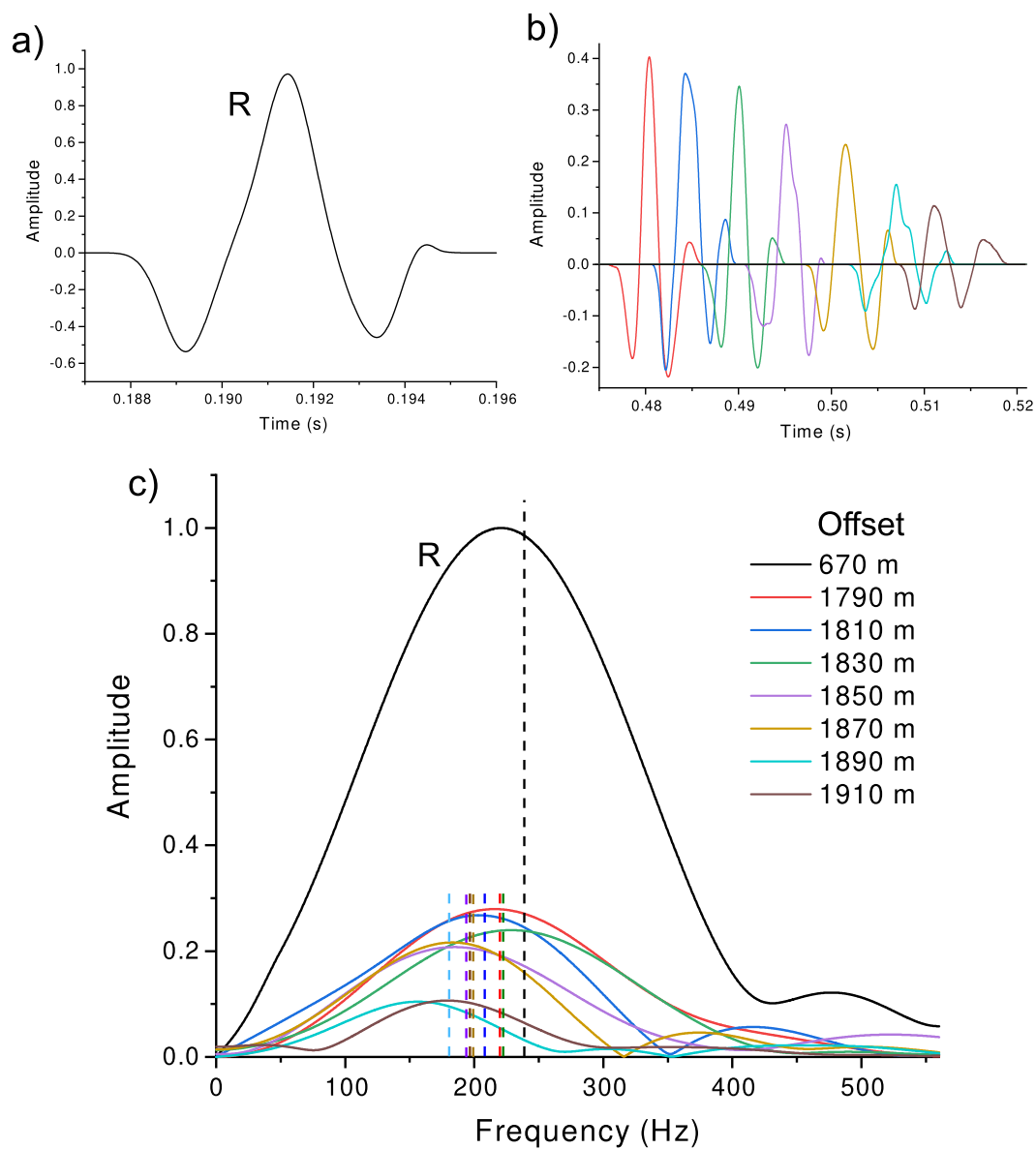

Figure 8. P-wave quality factor and dominant frequency versus depth, obtained from the layer-stripping frequency-shift method.
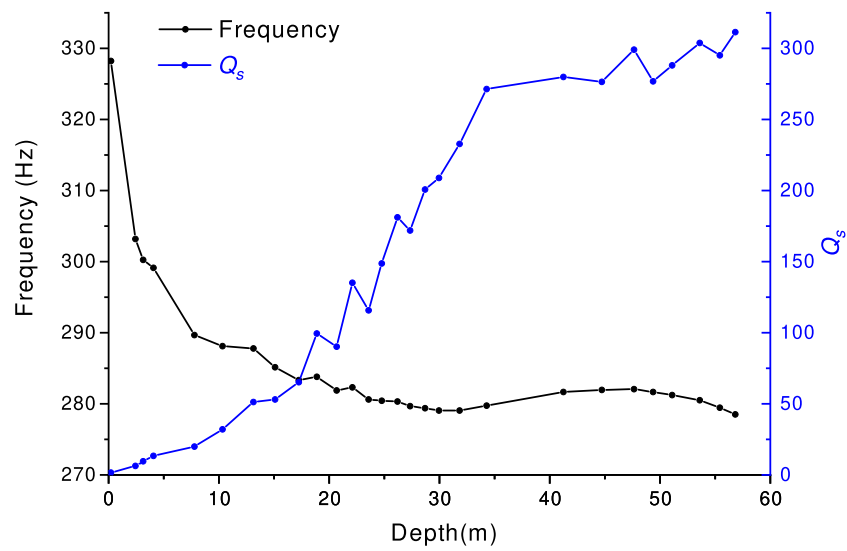
Figure 9. S-wave quality factor and dominant frequency versus depth, obtained from the layer-stripping frequency-shift method.
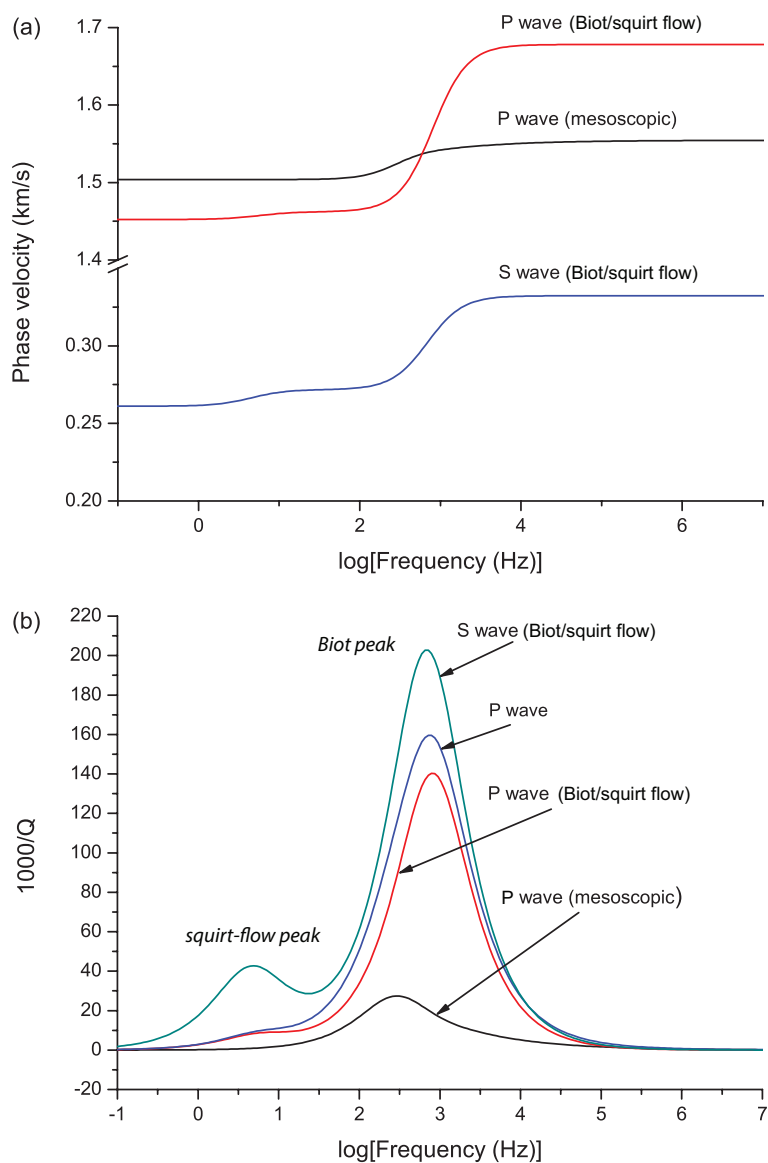
Figure 10. Wavelets (b) and corresponding spectra (c) of the P-wave first breaks recorded at long offset, between 1790 and 1910 m. The label R indicates the reference signal (a) recorded at 670 m offset, while the vertical dashed lines indicate the frequency centroids.

The Cryosphere
Discussions

a)

b)
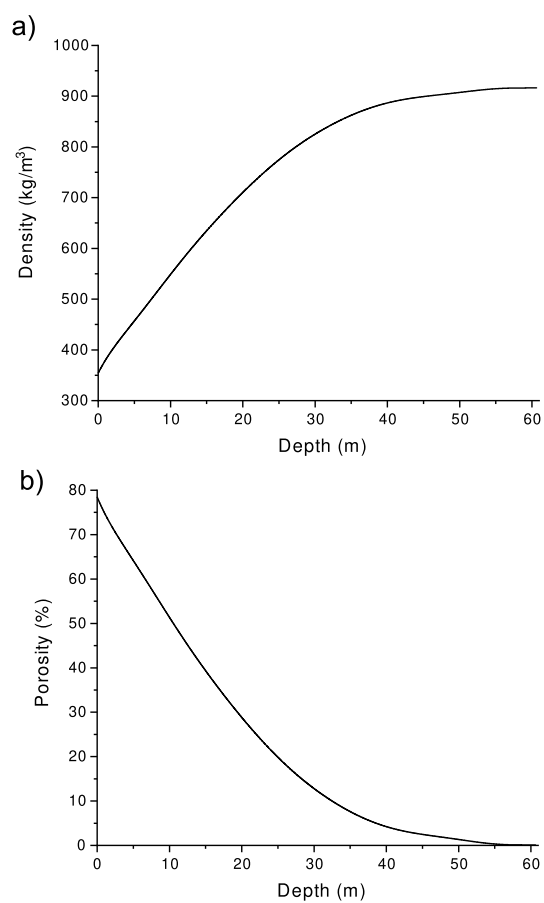
Figure 11. Density (a) and porosity (b) as a function of depth.

Figure 12. Analytical P-wave velocity (a) and dissipation factor (b) as a function of frequency close the surface.
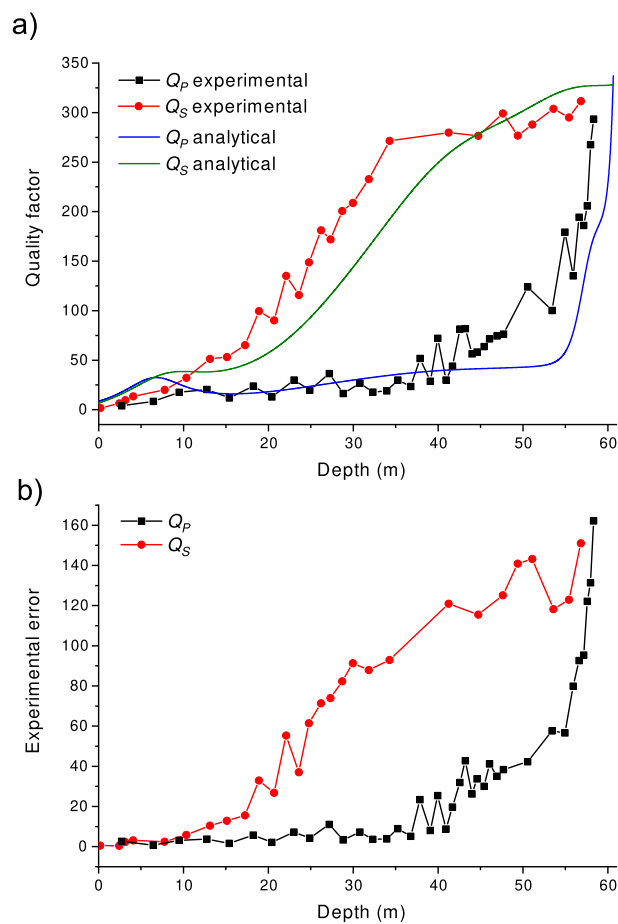
Figure 13. Comparison between the experimental (symbols) and theoretical (solid lines) P- and S-wave quality factors (a) as a function of depth. Experimental errors (b) in the computation of Q_P and Q_S from the layer-stripping frequency-shift method.